Title
Dynamics of creeping landslides controlled by inelastic hydro-mechanical couplings

Authors
Li, Xiang
Chen, Yanni
Handwerger, Alexander L
et al.

Publication Date
2023-05-01

DOI
10.1016/j.enggeo.2023.107078

Dynamics of Creeping Landslides Controlled by Inelastic Hydro-Mechanical Couplings

Xiang Li[1], Yanni Chen[1], Alexander L. Handwerger[2,3] and Giuseppe Buscarnera[1]

[1] Department of Civil and Environmental Engineering, Northwestern University, Evanston, USA.

[2]Jet Propulsion Laboratory, California Institute of Technology, Pasadena, USA.

[3]Joint Institute for Regional Earth System Science and Engineering, University of California, Los Angeles, Los Angeles, USA.

Abstract

Slow-moving landslides affect proximal infrastructures and communities, often causing extensive economic loss. While many of these landslides exhibit slow and episodic sliding for decades or more, they sometimes accelerate rapidly and fail catastrophically. Although it is known that the landslide dynamics are controlled by hydro-mechanical processes, few analytical models enable a versatile incorporation of the inelastic behavior of the shear zone materials, thus hindering an accurate quantification of how their properties modulate the magnitude and rate of coupled fluid flow and landslide motion. To address this problem, we develop a simulation framework incorporating rainfall-induced, deformation-mediated pore-water pressure transients at the base of active landslides. The framework involves the computation of two sequential diffusion processes, one within an upper rigid-porous landslide block, and another within the inelastic shear zone. Although the framework can be linked to any elastoplastic constitutive laws, here we model landslide motion through an elastic-perfectly plastic frictional model, which enables us to account for standard properties of earthen materials such as elastic moduli, friction angle, dilation angle, and hydraulic conductivity. Numerical case studies relevant to slow-moving landslides in the California Coast Ranges show that the proposed formulation captures different temporal patterns of movement induced by precipitation. In each of the case, we achieved a relatively accurate match between data and simulations by incorporating positive dilation coefficients, which leads to spontaneous generation of negative excess pore-water pressure and self-regulating motion. Conversely, simulations with no dilation (hence, reflecting the approach of critical state) produce sharp acceleration, typical of

catastrophic runaway acceleration. Our findings encourage the use of the proposed framework in conjunction with constitutive laws tailored to site-specific geomaterial properties and data availability, thus favoring a versatile representation of the variety of creeping landslide trends observed in nature.

Key words: *slow-moving landslides, hydro-mechanical coupling, rainfall infiltration, constitutive models*

1. Introduction

Slow-moving landslides are phenomena which unfold over several years, often even decades, with major implications for the serviceability of infrastructures, the safety of communities, and the local economy (Nappo, et al., 2019; Lacroix et al., 2020). Most slow-moving landslides deform at low rates (< 1 m/year) but can cause severe damage over time (Mansour et al., 2011). Some of them can even experience catastrophic acceleration and lead to fatalities (Voight, 1978; Hendron and Patton, 1985). The mobilization of these landslides is governed by environmental factors, such as precipitation, which acts to modulate the effective stress conditions in the slope (Petley et al., 2005; Cascini et al., 2010; Oberender and Puzrin, 2016). Infiltration of water leads to pore-water pressure development, which decreases the effective normal stress and reduces the frictional strength of the landslide material. As an outcome, these types of landslides normally accelerate in the wet season and slow down or arrest in the dry season (Hilley et al., 2004; Cascini et al., 2010; Handwerger et al., 2013).

In conjunction with frictional shear modulated by rainfall infiltration, downslope sliding is also mediated by the tendency of geomaterials to undergo inelastic volume change. This volume change can alter fluid flow and pore-water pressure development under certain conditions (Belmans et al., 1983; Wu et al., 2016; Song et al., 2020). The role of volumetric deformation on the sliding behavior has been extensively documented through field and laboratory measurements (Iverson et al., 2000; Moore and Iverson, 2002; Agliardi et al., 2020) and numerical models (Iverson 2005; Soga et al., 2016; Bandara et al., 2016). These studies have shown that the interaction between water infiltration and material volume change (hydro-mechanical coupling) may play an important role in governing the dynamics of slow-moving landslides.

A variety of methods exist to model these hydro-mechanical couplings. Such approaches account for shear zone inelasticity in the coupled field equations solving for pore fluid mass and momentum balance (Zienkiewicz et al., 2000; McDougall and Hungr, 2004; Soga et al., 2016). Although these methods can be used to study landslides of any morphology and kinematics, most have relatively high computational costs, especially if a seamless link between slow hydrologic triggering and rapid post-failure movements is desirable and their dynamics unfolds over long time, of the order of years or decades. In order to reduce the computational costs of full-fledged numerical methods, analytical techniques can be used to identify the mechanisms underpinning landslide motion and explain the role of the mechanical properties of the shear zone material. For example, early contributions by Hutchinson (1986) emphasized the crucial relation between the dissipation of excess pore-water pressure (i.e., consolidation mechanisms) and the dynamics of downslope sliding. Such models, formulated to describe liquefiable soils displaying positive feedbacks between deformation and pore-water pressure growth, led to a sliding-consolidation framework able to infer landslide velocity and runout for a variety of initial conditions. Despite its many benefits, this approach does not account for the inelastic deformation of the materials during liquefaction, and therefore cannot explicitly resolve the triggering of a landslide and its role on the onset of catastrophic motion (Buscarnera and Whittle, 2012). A more profound link between landslide triggering and post-failure movement was later proposed by Iverson (2005), whose seminal work encompassed excess pore-water pressure change through basal flux boundary conditions mediated by material dilation/contraction. However, this model too did not fully resolve the effect of inelastic mechanisms mediated by the stress-strain nonlinearity, in that excess pore-water pressure dissipation was modeled via poroelastic protocols based on a constant diffusion coefficient. This assumption conflicts with the notion that inelastic deformation can lead to major

77 alterations of the shear zone diffusivity (Rice, 1975; di Prisco et al., 2015; Chen and Buscarnera,
78 2021). These coupled effects render the process inherently poroplastic, which implies that a stress-
79 strain constitutive law is necessary to quantify the timescale of excess pore-water pressure
80 dissipation within the shear zone, as well as the magnitude and rate of landslide motion resulting
81 from inelastic deformation.

82 In this paper, we account for inelastic deformation during the entire life cycle of landslide motion
83 by developing a sliding-consolidation framework enabling the straightforward use of constitutive
84 laws with any desired level of sophistication. Our approach ensures readily deployable, low
85 computational cost simulations and is based on that developed by Chen and Buscarnera (2022).
86 Specifically, the framework proposed here resolves rainfall infiltration within the active sliding
87 block, thus connecting ground surface precipitation to the deformation dynamics. For this purpose,
88 the model involves two sequential diffusion processes, one taking place within a layer of rigid-
89 porous landslide material (which serves as hydrologic forcing), and another occurring within the
90 inelastic shear zone (which affects generation and dissipation of excess pore-water pressure). First,
91 the model is tested with reference to simple synthetic scenarios of precipitation, illustrating its
92 performance in interpreting the interaction between matrix deformation and pore-water pressure
93 dissipation. Then, it is used to interpret recorded time histories of landslide motion at three
94 landslide sites located in the California Coast Ranges, USA.

95 **2. Model description**

96 Field evidence suggests that the deformation of creeping (i.e., slow-moving) landslides originates
97 from localized shear zones with thickness varying between several centimeters to a few meters
98 (Corominas et al., 2000; Leroueil, 2001; Puzrin and Schmid, 2011; Wen et al., 2017; Alonso, 2021).

In-situ monitoring show that for many slow-moving landslides the upper block slides downslope as a rigid body overriding the stable material underneath (e.g., bedrock) (Fig. 1a). When precipitation occurs, infiltration impacts, sequentially, the landslide material and the shear zone, generating corresponding pore-water pressure transients. As an outcome, under a constant total overburden, the effective normal stress decreases in response to the transient pore-water pressure rise (Fig. 1b) in accordance with Terzaghi's (1925) effective stress definition. The stress components of the shear zone material can be defined as:

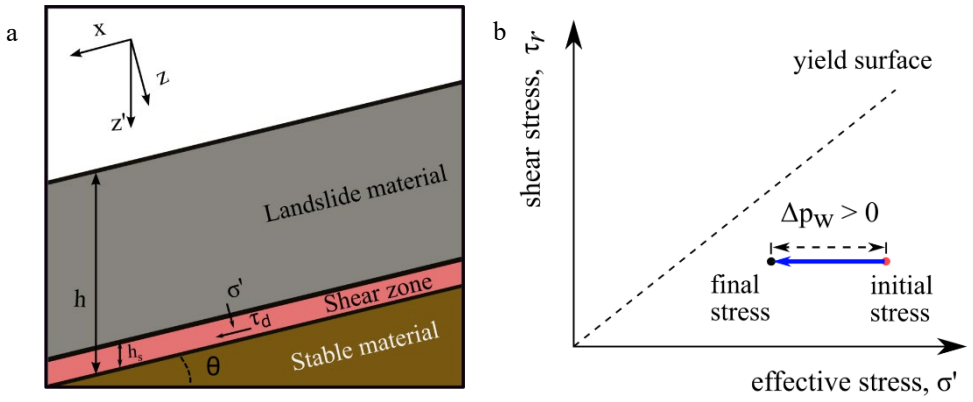

Figure 1. Schematic of slow-moving landslide slope profile and precipitation induced stress change. a) slope components under infinite slope geometry, b) material stress path induced by rainfall infiltration.

$$\sigma_d = \gamma_{sat} h cos^2\theta \,,$$

$$\tau_d = \gamma_{sat} h \sin\theta \cos\theta \,, \tag{1}$$

$$\sigma' = \sigma_d - p_w,$$

where σ_d and τ_d are the total normal stress and shear stress determined from the slope inclination θ, h is the thickness of the active sliding block (consists of landslide material and shear zone), and γ_{sat} is the saturated unit weight of the soil. σ' is the effective normal stress, and p_w is the pore-water pressure. Incorporating elastoplastic constitutive models for the shear zone material enables

116 the landslide dynamics to be analyzed by simulating the deformation in both the tangential and
117 normal direction caused by hydrologic processes.

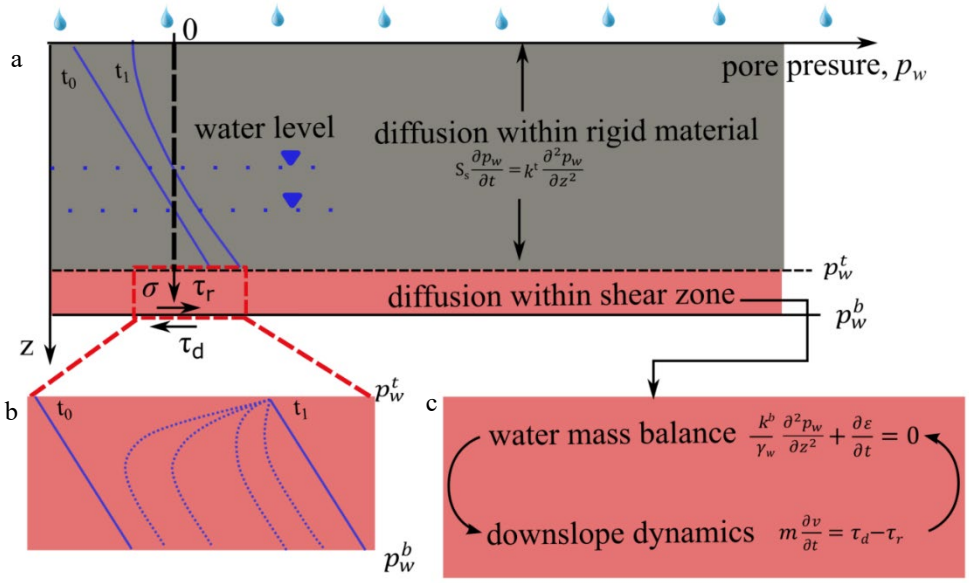

118

119 **Figure 2. Schematic of the 1D infinite slope model used for coupled hydro-mechanical analyses. a) Cross section**
120 **of the landslide material. The pore-water pressure distribution (solid blue line) of a normal profile (dashed**
121 **black line) and corresponding water level (horizontal blue dots) at different times. The governing equation for**
122 **the diffusion process inside the landslide material is also illustrated. b) Zoom of the shear zone. The solid lines**
123 **represent the stationary pore-water pressure induced by the pressure input on top of the shear zone, while the**
124 **dashed blue lines represent for possible pore-water pressure development mediated by the dilation as explained**
125 **in Sections 3.1 and 3.2. c) The governing equations for the diffusion process inside the landslide material.**

126 In this study, the hydro-mechanical equations controlling the dynamics of a creeping landslide are
127 set to address two separate diffusion processes: one within the upper landslide material, here
128 treated as a porous, rigid block; another within the inelastic shear zone (Fig. 2). The former
129 diffusion mechanism determines the main external loading, i.e., hydrological forcing for the basal
130 shear zone following the variation of water level and is solved with a previously developed 1D
131 Finite Element solver for infinite slopes (Lizarraga and Buscarnera, 2019; more details in Section

2.1). By contrast, the second diffusion mechanism controls the timescale of pore-water pressure development and dissipation in response to inelastic deformation within the basal shear zone. The corresponding hydro-mechanical couplings affect both diffusivity and deformability beneath the landslide mass, thus requiring the use of site-specific constitutive laws of the shear zone material (Sections 2.2 and 2.3).

2.1 Pore-water pressure diffusion within the landslide material

Here, we solve the water mass balance in the landslide material to determine the pore-water pressure transients induced by rainfall infiltration on top of the shear zone, which ultimately controls the hydro-mechanical coupling of the shear zone. These transients are computed on the basis of Eq. 2, where the diffusive effects are encapsulated into two constant parameters, the storage coefficient, S_s, and the saturated permeability of the landslide material, k^t, (e.g., Iverson, 2000; Berti and Simoni, 2010; Cohen-Waeber et al., 2018), as follows:

$$S_s \frac{\partial p_w}{\partial t} = k^t \frac{\partial^2 p_w}{\partial z^2}, \tag{2}$$

where z is the normal distance from the ground surface. In this manuscript, the above equation is solved through the numerical algorithm proposed by Lizárraga and Buscarnera (2019). For the sake of simplicity, the hydrologic triggering is simulated by imposing flow (infiltration) conditions at the top of the landslide material and an impervious boundary at its bottom due to the impermeable bedrock below the shear zone (Baum et al., 2010). While more general analyses accounting for permeability contrasts can be carried out (Lizarraga and Buscarnera, 2019), this simplification has limited qualitative bearing on the analyses shown in this paper and will therefore be used as a convenient working hypothesis.

We simulate dry and wet seasonal changes that are typical of sites in California (Swain, 2021), which is the focus area of our research. During the simulated wet season, we apply a surface flux boundary condition equivalent to the precipitation. Water run-off was not considered, but its incorporation is straightforward, if needed, by accounting for moisture change at the surface (Song et al., 2021). Finally, to capture the widely observed sequence of pore-water pressure rise during the wet season, followed by its decrease during the dry season (e.g., Iverson and Major, 1987; Schulz et al., 2018a; Finnegan et al., 2021), pressure boundary conditions were imposed at the top of the slope during periods with no rainfall.

2.2 Coupled flow-deformation within the shear zone

Within the shear zone, coupled flow-deformation processes can be simulated by analyzing the downslope dynamics and water mass balance simultaneously (Chen and Buscarnera, 2022). In this portion of the slope, the initial stress state is altered by the interaction between water flow and deformation. From a mechanical viewpoint, the downslope dynamics implies:

$$ma = \tau_d - \tau_r, \tag{3}$$

where $m = \rho_s h cos\theta$, is the total mass of the active sliding block, a, its acceleration, τ_d, the driving shear stress (Eq. 1), τ_r, the resisting stress, here regarded as a function of the local constitutive response, as follows:

$$\dot{\tau}_r = G(\dot{\gamma} - \dot{\gamma}^p);\ \dot{\sigma}' = E_{oed}(\dot{\varepsilon} - \dot{\varepsilon}^p). \tag{4}$$

where G is the elastic shear stiffness, E_{oed} is elastic oedometric modulus. ε and ε^p are the total and plastic normal strain; γ and γ^p are the total and plastic shear strain. Eq. 4 involves both shear stress and the effective normal stress; the latter is indeed a function of the normal strain and controlled by volume change. As it will be discussed below in Section 2.3, plastic strain increments

175 can be computed with constitutive models. Here, to link the shear strain to the landslide movement,
176 the shear strain rate, $\dot{\gamma}$, is computed by assuming a linear velocity (v) profile within the shear zone
177 in z direction (MiDi, 2004; Pastor et al., 2015; Siman-Tov and Brodsky, 2021), as follows:

178 $$\dot{\gamma} = \frac{v}{h_s cos\theta}, \tag{5}$$

179 where h_s represents the thickness of the shear zone (Fig. 1a). This choice enables us to use Eq. (3)
180 ~ (5) to derive the following sliding equation:

181 $$\rho_s h cos\theta \ddot{v} = \dot{\tau}_d - G\frac{v}{h_s cos\theta} + G\dot{\gamma}^p, \tag{6}$$

182 where ρ_s is the saturated density of soil. The effective normal stress change in Eq. 4 must follow
183 the rates of volume change compatible with the water mass balance in the shear zone. Here, this
184 process is simulated by treating the fluid as incompressible and considering the rate of volume
185 change as the only source of diffusive feedbacks within the shear zone (Sloan and Abbo, 1999;
186 Mihalache and Buscarnera, 2016), as follows:

187 $$\frac{k^b}{\gamma_w}\frac{\partial^2 p_w}{\partial z^2} + \dot{\varepsilon} = 0, \tag{7}$$

188 where k^b is the saturated permeability of the shear zone material, and γ_w is the unit weight of
189 water. The normal strain rate consists of elastic and plastic deformation rates ($\dot{\varepsilon} = \dot{\varepsilon}^e + \dot{\varepsilon}^p$).
190 Therefore, we can rewrite Eq. 7, as follows:

191 $$\frac{k^b}{\gamma_w}\frac{\partial^2 p_w}{\partial z^2} + \frac{\dot{\sigma}_d - \dot{p}_w^b}{E_{oed}} + \dot{\varepsilon}^p = 0, \tag{8}$$

192 from which it is readily apparent that the inelastic volume change regulates the pressure diffusion
193 process across the shear zone.

In our model, the time varying pore-water pressure input, $\dot{p}_w^t$, at the boundary between the landslide material and shear zone (here computed through the uncoupled diffusion analysis in Eq. 2) will serve as a forcing in Eq. 8, which is aimed at computing the change of the pore-water pressure at the bottom of the shear zone ($\dot{p}_w^b$). While Eq. 8 is a second order partial differential equation (PDE), a parabolic approximation of the excess pore-water pressure (p_w^e) profile compatible with analytical solutions of soil consolidation (Wood, 2004) is here used to condense the analysis of the landslide dynamics to an ordinary differential equation (ODE) that can be solved with numerical and/or analytical solutions. Specifically, use of a parabolic pressure profile implies (equation derivation see Appendix 1):

$$\frac{\partial^2 p_w}{\partial z^2} = \frac{2(p_w^{sb} - p_w^b)}{h_s^2 cos^2\theta}, \tag{9}$$

where p_w^{sb} represent the stationary (steady state) pore-water pressure at the bottom of shear zone corresponding to a hydrological forcing applied on the top of the shear zone ($p_w^{sb} = p_w^t + h_s cos\theta \gamma_w$, and $\Delta p_w^t = \Delta p_w^{sb}$), p_w^b is the pore-water pressure at the bottom of the shear zone. Combining Eq. 9 with Eq. 7, we can then define a set of coupled governing equations conveying the effect of the inelasticity of the shear zone material on the landslide dynamics as follows:

$$\dot{p}_w^b = \frac{2E_{oed}k^b}{\gamma_w h_s^2 cos^2\theta}(p_w^{sb} - p_w^b) + E_{oed}\dot{\varepsilon}^p + \dot{\sigma}_d, \tag{10a}$$

$$\rho_s h cos\theta \ddot{v} = -G\frac{v}{h_s cos\theta} + G\dot{\gamma}^p + \dot{\tau}_d. \tag{10b}$$

The solution to Eq. 10 can be addressed once their inelastic deformation terms are specialized with constitutive models.

2.3 Constitutive models

While an extensive number of constitutive relations for earthen material is nowadays available, a natural choice for a specialized form of the proposed framework is a perfectly plastic frictional law (Davis and Selvadurai, 2005). In fact, such a constitutive choice enables simplicity and straightforward identification of model parameters for a variety of landslide case studies (Van Asch et al., 2007; Corominas et al., 2005; Conte et al., 2014; Schulz et al., 2018a). In the case of frictional plasticity, we define:

$$f = \tau - \sigma' tan\varphi, \qquad g = \tau - \sigma' tan\psi, \tag{11}$$

where f and g are a yield function and a plastic potential, respectively. φ is the friction angle and ψ represents the dilation angle. In this scenario, the plastic deformation rate in both normal and tangential directions can be obtained as:

$$\dot{\varepsilon}^p = \Lambda \frac{\partial g}{\partial \sigma'};\ \dot{\gamma}^p = \Lambda \frac{\partial g}{\partial \tau_r}, \tag{12}$$

where Λ is the plastic multiplier (i.e., a scalar that accounts for the magnitude of plastic effects) determined by the consistency condition of the yield surface. By using effective normal stress and shear strain as control parameters (Buscarnera et al., 2011), it follows that:

$$\Lambda = \frac{1}{H - H_2}\left(\frac{\partial f}{\partial \sigma'}\dot{\sigma}' + \frac{\partial f}{\partial \tau_r} G\, \dot{\gamma}\right), \tag{13}$$

where H is the hardening modulus, H_2 is a plastic modulus determined by the control conditions used to quantify plastic effects. Based on Eq. 11, the plastic moduli can be expressed as:

$$H = 0;\ H_1 = -\frac{\partial f}{\partial \sigma'} E_{oed} \frac{\partial g}{\partial \sigma'} = -tan\varphi E_{oed} tan\psi;\ H_2 = -\frac{\partial f}{\partial \tau_r} G \frac{\partial g}{\partial \tau_r} = -G. \tag{14}$$

Here, $H = 0$ in that the selected constitutive law is perfectly plastic. Introducing Eq. 14 into Eq. 13 and combining the result with Eq. 10, the complete set of coupled governing equations based on the selected constitutive law is:

$$\dot{p}_w^b = \frac{k^b E_{oed}}{\gamma_w} \frac{2(p_w^{sb} - p_w^b)}{h_s^2 cos^2\theta} A + B \frac{1}{tan\varphi} \frac{Gv}{h_s cos\theta} + \dot{\sigma}_d \,, \tag{15a}$$

$$\rho_s h cos\theta \ddot{v} = \frac{k^b E_{oed}}{\gamma_w} \frac{2(p_w^{sb} - p_w^b)}{h_s^2 cos^2\theta} A \, tan\varphi - B \frac{Gv}{h_s cos\theta} + \dot{\tau}_d \,, \tag{15b}$$

where A and B are plastic coefficients expressed as $A = \frac{G}{G + tan\varphi E_{oed} tan\psi}$, and $B = \frac{tan\varphi E_{oed} tan\psi}{G + tan\varphi E_{oed} tan\psi}$, respectively. From Eq. 15, we can compute the interaction between shear zone hydraulic flow and mechanical deformation when rainfall infiltration occurs.

2.4 Nondimensionalization

It is often beneficial to identify nondimensional timescales controlling dynamic systems because it helps us understand the relation between distinct timescales involved in our study such as rainfall infiltration and material consolidation. Also, it can reduce the complexity of the governing equations and reveal the key parameters needed to understand complex physical processes. In this study, standard nondimensionalization strategies are used (Tan, 2011). This involves rescaling the system variables by normalizing them for a reference quantity, here denoted through an overhead hat (e.g., $\hat{t}$ for a reference time). On such basis, the normalized quantities can be displayed through an overhead tilde (e.g., $\tilde{t}$ for normalized time, equals to $t/\hat{t}$). Selection of reference quantities with clear physical meaning facilitates the identification of the underlying mechanics. Here, the reference time is selected as the duration of forcing ($\hat{t} = T$), while other reference quantities are $\hat{\sigma} = \hat{p}_w = \sigma_0 = \gamma_s h cos^2\theta, \hat{\tau} = \tau_0 = \tan\theta \, \sigma_0, \hat{a} = \tau_0/\rho_s h cos\theta, \hat{v} = \hat{a}\hat{t}$.

Accordingly, the governing equation (Eq. 15) can be re-written as:

$$\dot{\tilde{p}}_w^b = 2T_{lc}^e A(\tilde{p}_w^{sb} - \tilde{p}_w^b) - B\frac{tan\,\theta}{tan\,\psi}T_{lw}^e\tilde{v} + \dot{\tilde{\sigma}}_d\,, \tag{16a}$$

$$\ddot{\tilde{v}} = 2T_{lc}^e A\frac{tan\,\psi}{tan\,\theta}(\tilde{p}_w^{sb} - \tilde{p}_w^b) - BT_{lw}^e\tilde{v} + \dot{\tilde{\tau}}_d\,, \tag{16b}$$

where $T_{lc}^e = \frac{E_{oed}k^bT}{\gamma_w h_s^2 cos^2\theta}$, is the ratio of total forcing time divided by the characteristic consolidation time for an elastic material, which controls the shear zone hydraulic diffusion when it deforms elastically. In addition, considering the standard expression of the shear wave velocity in an elastic medium, $v_s^e = \sqrt{G/\rho}$, it is possible to define a reference time for a shear wave to travel across the active sliding block ($\tilde{t}_h$) and the shear zone ($\tilde{t}_{hs}$) as:

$$T_{lw}^e = (\tilde{t}_h\tilde{t}_{hs})^{-1} = \frac{GT^2}{\rho h h_s cos^2\theta}\,. \tag{17}$$

Therefore, the coupled behavior of a creeping landslide inside the shear zone involves a number of controlling nondimensional parameters dictating its dynamics, including the diffusion time (T_{lc}^e), the shear wave propagation time (T_{lw}^e), the slope inclination (θ), and the elastoplastic properties encapsulated into the plastic coefficients A and B.

3. Model performance

3.1 Precipitation-induced diffusion and elastic response

To explore our model's ability to simulate landslide movements induced by precipitation, the model is first tested with an artificial (and unrealistic) rainfall event, which lasts for 30 days (T) with a constant intensity (q). While the analysis is purely illustrative, the range of model parameters is chosen on the basis of landslide sites in the California Coast Ranges (Keefer and

Johnson, 1983; Kelsey et al., 1996). Hence, the rainfall intensity is set equal to the saturated permeability of landslide material (k^t), here assumed to be 3x10^{-6} m/s (according to measurements from Iverson and Major, 1987) and the storage coefficient (S_s) is set to 0.26. The pore-water pressure change at the interface between the landslide material and the active shear zone (Δp_w^t i.e., Δp_w^{sb}) can be computed numerically. The results are provided in Fig. 3a, which shows that the p_w^t increases monotonically after the wetting front approaches the top of the shear zone when $\tilde{t}$ is around 0.3.

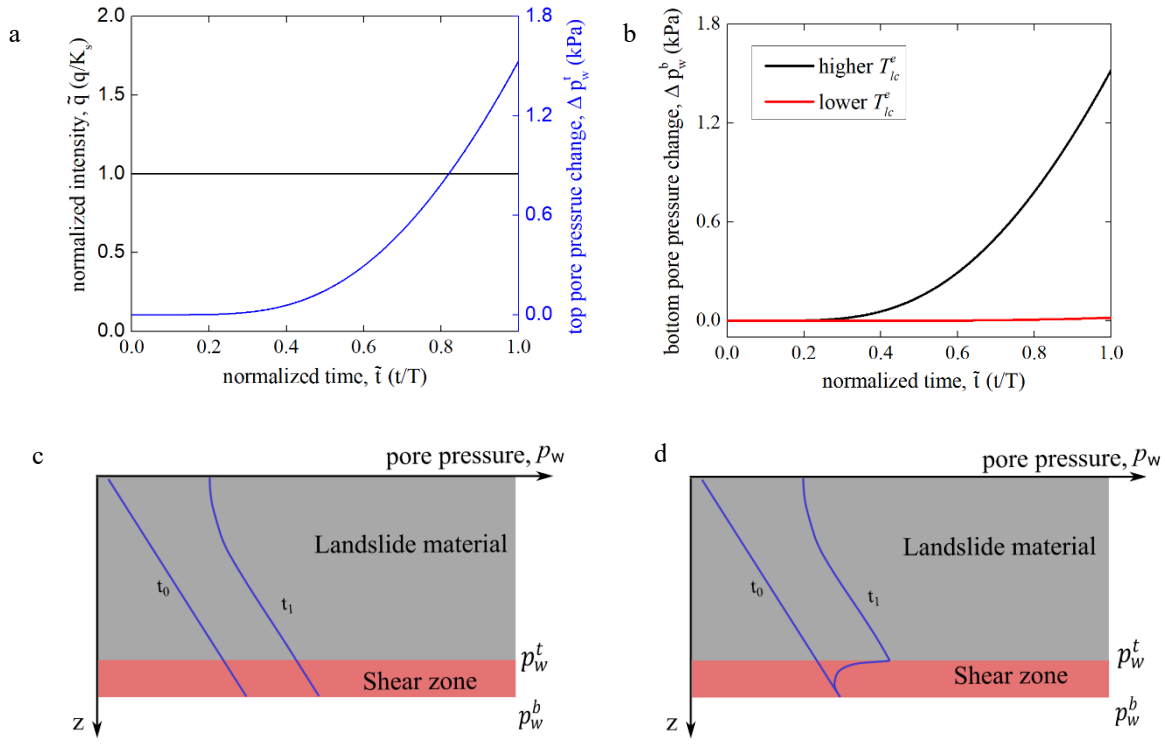

Figure 3. Simulation of pore-water pressure transients caused by precipitation. a) Simulated pore-water pressure change at top of shear zone caused by a constant rainfall. b) Computational results of pore-water pressure change at bottom of shear zone, corresponding to different value of T_{lc}^e; c & d) schematics of pore-water pressure distribution with higher and lower T_{lc}^e, where higher T_{lc}^e results from shear zone permeability (k^b) 5.5 x10^{-7} m/s, and lower T_{lc}^e indicate k^b =5.5 x10^{-12} m/s. The thickness of the landslide material is 20m. Stiffness parameters are taken as: oedometric modulus E_{oed} = 5 MPa, and shear modulus G = 2 MPa.

285 The computed p_w^t will then serve as the hydraulic boundary condition activating coupled behavior
286 inside the deformable shear zone. Simulations are conducted for different values of T_{lc}^e (Eq. 16) to
287 examine its role on pore-water pressure diffusion processes within the shear zone. In this study,
288 T_{lc}^e depends on the value of the hydraulic conductivity, k^b, as discussed in the previous section.

289 Fig. 3b shows that, when T_{lc}^e is relatively high, diffusion takes place rapidly within the shear zone,
290 thus the hydraulic response (Δp_w^b) at the bottom of the shear zone follows the hydrologic forcing
291 (Δp_w^t, i.e., Δp_w^{sb}). The pore-water pressure profile in this scenario is illustrated in Fig. 3c. On the
292 contrary, pore-water pressure change can be delayed in the shear zone in the presence of low T_{lc}^e
293 values. This is illustrated in Fig. 3d, where the pore-water pressure at the bottom of the shear zone
294 barely changes despite the application of a hydrological forcing at the top of the deformable zone.
295 Since these tests are conducted for landslide material under an elastic regime, infiltration does not
296 involve approaching of the yield surface and mobilization of the plastic resources of the shear zone.
297 As an outcome, no sliding is generated.

298 *3.2 Model behavior under the plastic regime*

299 When the fluctuations of the effective stress state induced by infiltration are large enough to engage
300 the frictional yield surface, plastic shear strain and consequent sliding occur. Separating from the
301 elastic regime, the material yield surface also starts to regulate the stress changes and
302 corresponding deformation. For example, if the material dilation angle (ψ) is zero, no negative
303 excess pore-water pressure can be generated. In this context, the pore-water pressure increase will
304 be the same as triggered by water diffusion in the elastic regime (Fig. 1b). Yet, under the
305 elastoplastic framework, the yield surface cannot be surpassed. The pore-water pressure increase
306 will thus lead to stress changes along the yield surface (Fig. 4a). As an outcome, the shear zone

material will lose strength (Eq. 3), and runaway failure can be triggered. Most notably, if non-zero plastic normal deformation is developed, negative excess pore-water pressure will be induced and regulate the slope dynamics. Plastic dilation, if prevented, will generate negative excess pore-water pressure (Fig. 4b), which, in order not to violate the prescribed strength criterion and sustain the initial shear stress level, must be opposite and equal to the pressure change induced by infiltration (Fig. 1b). Specifically, since in our analyses the shear zone material has low permeability, diffusion within the basal sliding tends to progress slowly. Consequently, the increase of the bottom pore-water pressure induced by infiltration is small and its value is affected by the abovementioned negative excess pore-water pressure controlled by the dilative response of the material. Most importantly, to comply with the strength characteristics underlying the selected perfectly plastic MC constitutive law (i.e., a fixed yield surface), the resulting basal pore-water pressure and the corresponding effective stress will be such that the material remains on a state of plastic sliding throughout the forcing process, with the pore pressure decreasing only when the rainfall stops, the material returns in a poroelastic state, and the excess pore-water pressure fully dissipates until the landslide movement ceases. These arguments show that dilation generates self-regulating effects

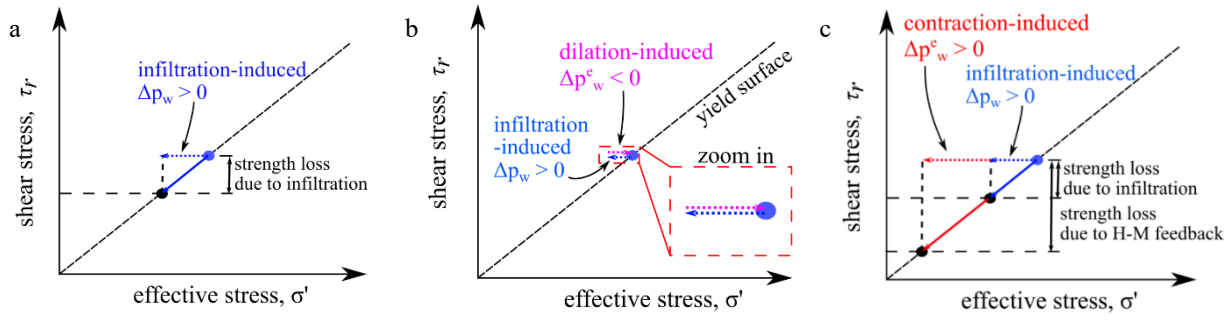

Figure 4. Schematics of effective stress paths at the base of a landslide predicted by the proposed framework for movements induced by hydrologic forcing. a) Stress change caused by hydrological forcing in plastic regime with nil normal plastic deformation. b) Dilative material generated self-regulating behavior. c) Contractive material induced self-feeding mechanisms.

able to constrain the pore-water pressure build-up. In contrast, contractive deformation would lead to an opposite outcome, by generating positive excess pore-water pressure and adding to the infiltration effects (Fig. 4c), eventually leading to more strength loss and runaway failure.

For our first landslide simulation in the plastic regime, we model landslide motion with dilative material. We apply a simple synthetic pore-water pressure event distributed normally with a magnitude of around 11 kPa over one year ($T = 365$ days) at the top of the shear zone to represent pore-water pressure changes expected during a water cycle consisting of wet season (e.g., Finnegan et al., 2021) and following dry seasons in California (Fig. 5). The T_{lc}^{e} (k^b = 3x10^{-9} m/s) is set to cause nearly instantaneous pore-water pressure change (Fig. 5a). The small values of k^b used in the analyses reflect the low permeability often reported for shear zone materials of the study sites (Baum and Ried, 2000; Nereson et al., 2018). When $\varphi = 20°$, the material yield surface is not approached and there is only elastic deformation. In contrast, a lower friction angle ($\varphi = 16°$) leads to plastic shearing (Fig. 5a & b, point B' to B'') under the same hydrological forcing.

Fig 5a and b show that, for $\varphi = 16°$, plasticity ensues when the imposed pore-water pressure at the top of the deformable zone is close to 8 kPa (i.e., point B', at $\tilde{t}$ = 0.4). Subsequently, plastic deformation begins to develop in both normal (induce volume change) and tangential directions (trigger downslope sliding, Fig. 5b). Regulated by plastic dilation, negative excess pore-water pressure is generated which prevents further pore-water pressure change. As explained in the previous example (Fig. 4b), the self-regulating effect halts the growth of pore-water pressure (Fig. 5f) and prevents the landslide from losing strength and accelerating catastrophically.

When the pore-water pressure applied at the top of the shear zone begins to drop and drives the material back into the elastic regime (point B'', $\tilde{t}$ = 0.6), the pore-water pressure at the bottom of

the shear zone decreases and there is a transition from the plastic to elastic domain. At the same time, sliding stops (Fig. 5b point B''), marking the end of the episodic development of negative excess pore-water pressure coupled with downslope sliding. For the case with $\varphi = 20°$ (Fig. 5 a, c, e), the whole process is in the elastic regime and there is no sliding nor negative excess pore-water pressure (Fig. 5b). These results confirm that sliding occurs only if precipitation mobilizes the inelastic resources of the shear zone material. Most notably, our model shows (similar to other studies) that dilation in the plastic regime leads to self-regulated landslide motion.

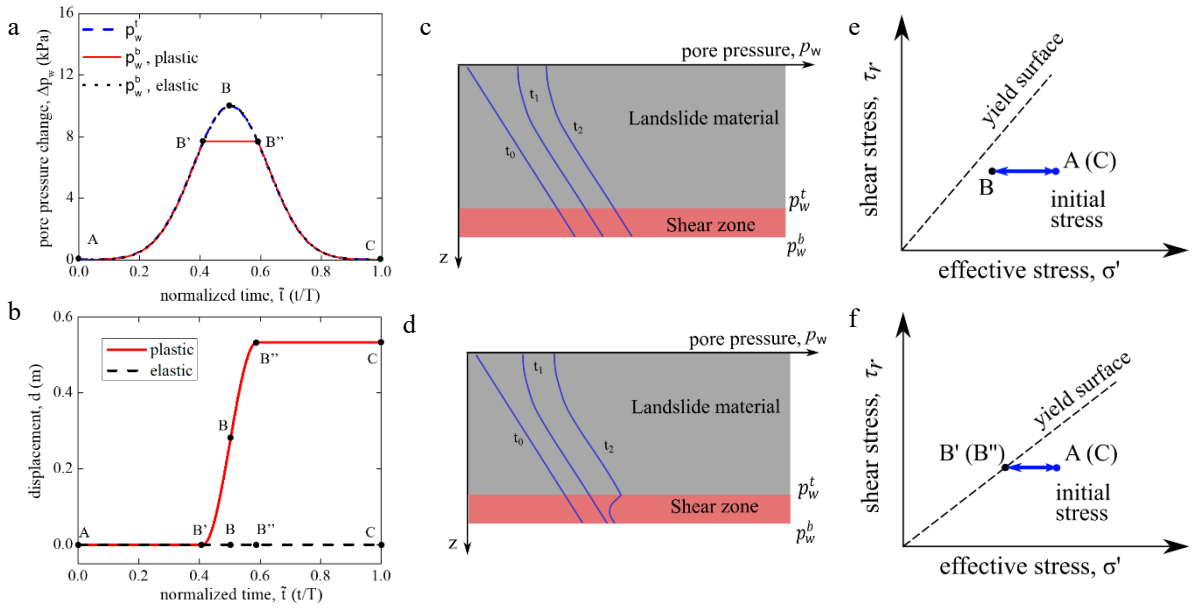

Figure 5. Simulation of the hydro-mechanical response of an infinite slope subjected to imposed pore-water pressure change at the top of its shear zone. A) top shear zone pore-water pressure changes in one year, with the bottom response under both the elastic and plastic regime. b) Downslope displacement, c & d) pore-water pressure profile when material is under the elastic and plastic regime. e & f) Schematic of hydrological response in elastic and plastic regime. Synthetic slope tested here is assumed to be thickness, h-h_s = 7 m (h_s = 0.5 m), slope angle θ = 15°, and dilation angle $\psi = 2°$.

3.3 Coupling effects

364 The dilation angle ψ governs the ratio of normal deformation divided by the sliding deformation.
365 To further investigate its effects, the same synthetic slope and pore-water pressure variation
366 illustrated in Fig. 5 are tested with different values of ψ (5°, 2°, and 0°), but equal friction angle
367 (φ =16°). Among the tested cases, $\psi = 0°$ is used to explore the landslide behavior for vanishing
368 dilation (i.e., potential approach of critical state conditions).

369 Fig. 6a shows that pore-water pressure at the bottom of the slope predicted for cases with dilative
370 deformation (i.e., $\psi > 0$) ceases to increase following the hydrological forcing, thus leading in all
371 cases to self-regulating effects. In contrast, these self-regulating effects vanish in the analyses
372 conducted with $\psi = 0°$ and runaway failure occurs. Our model simulations also indicate the pore-
373 water pressure stops changing in the plastic regime because the positive pore-water pressure
374 caused by infiltration is balanced by the negative excess pore-water pressure that results from
375 dilation as discussed above (Fig. 4b). In other words, for the perfectly plastic behavior inherent
376 with the MC constitutive law used in the current analyses, once the yield surface is reached, the
377 pore-water pressure will experience no further change (increase or decrease) until the seasonal
378 infiltration ends. Yet the dilation angle does impact the overall landslide displacement because it
379 represents the ratio of normal dilation divided by downslope sliding. As Fig. 6b displayed, the
380 same amount of dilative normal deformation would be triggered with a positive ψ (to induce the
381 negative pore-water pressure to balance the infiltration induced pore-water pressure increase).
382 While as ψ quantifies the normal dilation divided by sliding, under same amount of dilation, the
383 higher the ψ, the smaller the sliding will be induced. As Fig. 6c illustrated, for a dilation angle of
384 5°, the simulated sliding displacement is around 0.2 m. This movement more than doubles for ψ
385 = 2°, reaching more than 0.5 m.

When $\psi = 0°$, no dilation would be triggered (Fig. 6b). As an outcome, no negative excess pressure can act to prevent runaway acceleration (Fig. 6c). The same analysis can be conducted for shear zone materials experiencing contraction (i.e., $\psi<0$). This scenario mimics so-called liquefaction effects, i.e., self-feeding growth of excess pore-water pressure accompanied by loss of shearing resistance (Iverson, 2005; Iverson and George, 2014; Chen and Buscarnera, 2022). The sharp transition between these different landslide dynamic regimes is qualitatively illustrated in Fig. 6d. While the incorporation of multiple nonlinear constitutive laws is necessary to simulate the abrupt development of excess pore-water pressure and high mobility failure events such as liquefaction, it is beyond the scope of this paper.

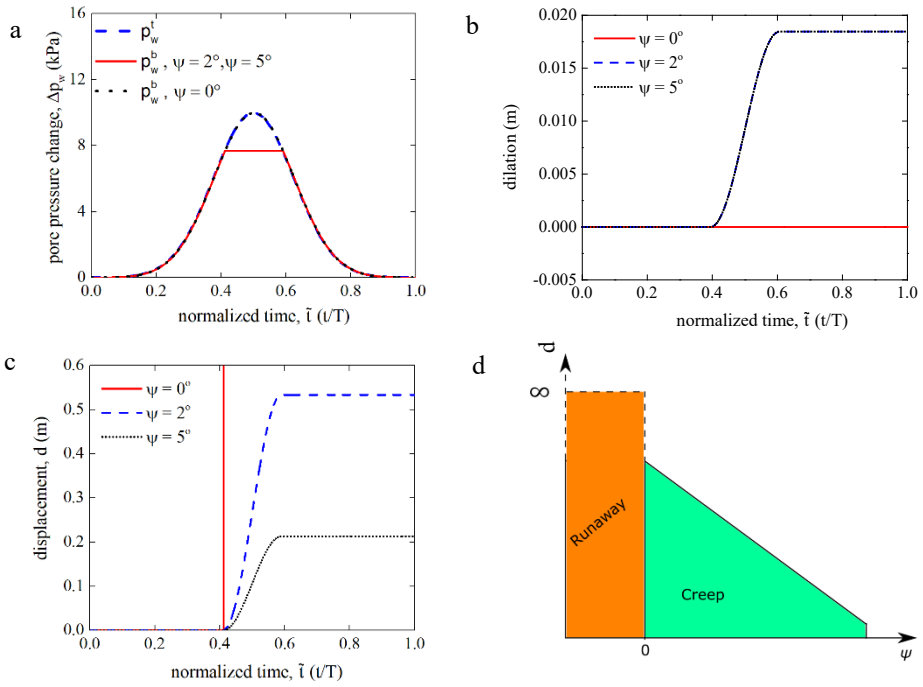

Figure 6. Simulation of the hydro-mechanical response of infinite slopes with basal shear zone characterized by different dilation angles. a) pore-water pressure at the top and bottom of the shear zone, b) computed normal dilation, c) simulated displacement, d) relationship between sliding displacement after the hydrological pulse and dilation angle, including cases leading to runaway failure.

4. Case studies

4.1 Sites of interests

There are thousands of landslides in the California Coast Ranges (Keefer and Johnson, 1983; Kelsey et al., 1996; Bennett et al., 2016; Handwerger et al., 2019b; 2022). Landslides occur in this region due to active tectonics, mechanically weak rocks, and high precipitation (Scheingross et al., 2013; Roering et al., 2015). The precipitation in California is seasonal and most falls during the wet season between October and May (Swain, 2021). Most of the slow-moving landslides occur within the Jurassic-Cretaceous Franciscan Mélange (Fig. 7, referred to as "KJf"). The KJf is a clay-rich complex unit made of sandstone, shales, serpentinite, and conglomerates (Bailey et al., 1964; Rutte et al., 2020).

For our model simulations, we selected parameter value ranges for friction angle, permeability, and dilation angle from previously published studies (Keefer and Johnson, 1983; Vermeer and de Borst, 1984; Iverson and Major, 1987; Roadifer et al., 2009; Nereson et al., 2018) on landslides in the CA Coast Ranges (details in Section 4.2). However, for stiffness parameters that were not measured at these sites, we used reasonable approximations for clay-rich compositions (Obrzud, 2010): oedometric modulus, E_{oed} = 5 MPa, and shear modulus, G = 2 MPa.

We selected three landslide sites to test our model: 1) Two Towers landslide, northern California (Schulz et al., 2018a; b), 2) Minor Creek landslide, northern California (Iverson and Major, 1987), and 3) Mud Creek landslide, central California (Handwerger et al., 2019). Hourly movement of Two Towers landslide was measured from 11 November 2014 to 22 July 2017 using a biaxial tilt sensor (Schulz et al., 2018a; b). The Minor Creek landslide was monitored between 1982 and 1985

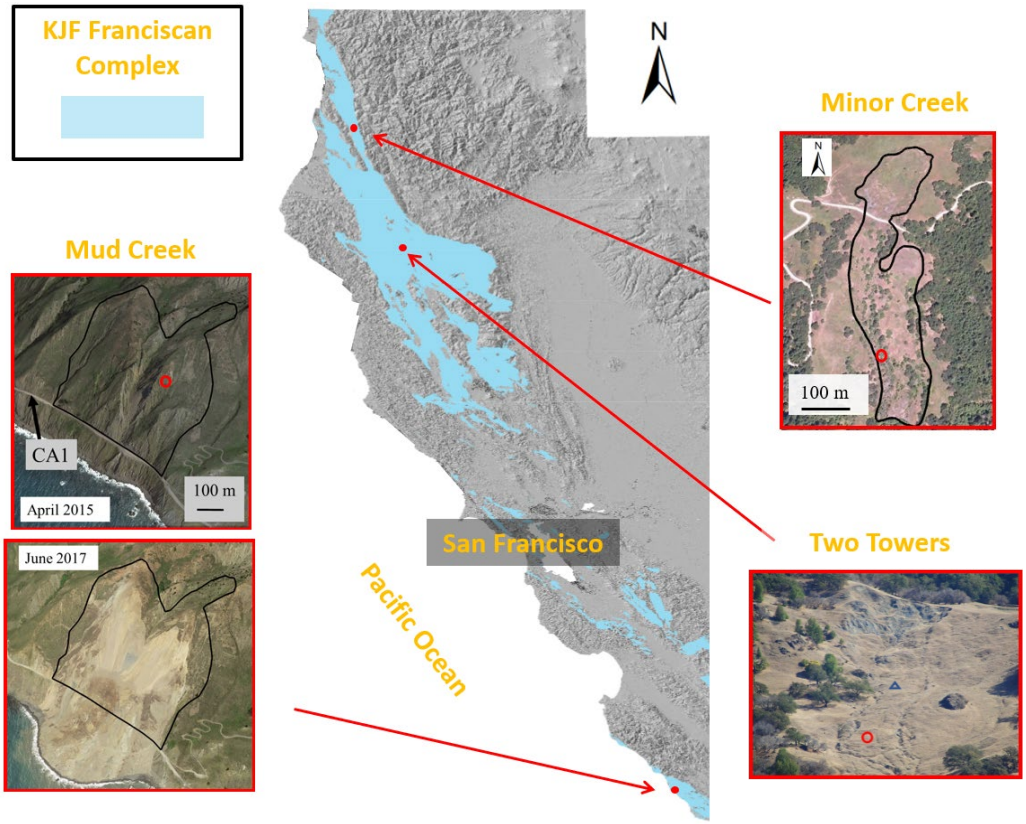

Figure 7. California Coast Ranges and Franciscan Complex lithologic unit 1 draped over a hillshade of the topography with labeling and location details of the landslide sites studied in this paper (the monitoring points at which each landslide displacement was measured are circled, and the water level monitoring location of Two Towers landslide is shown by triangle).

using extensometers (Iverson and Major, 1987). Finally, the Mud Creek landslide was monitored between 2015 and 2017 (Handwerger et al., 2019a) through satellite interferometric synthetic aperture radar (InSAR). In this study, the analyses are based on a 1D infinite slope geometry, in that the length of the considered landslides are much higher than their width and depth. This implies that the landslide is a uniform block of constant inclination with movements that do not vary along the downslope direction. This widely used simplification is applicable to capture the overall kinematics of the landslide (Angeli et al., 1996; Iverson, 2005; Van Asch et al., 2007; Li et al., 2021), but it might suffer a loss of accuracy at the edges of the domain, especially in regions

of extension and/or compression which require a 2D or 3D model of the slope geometry. Notably, we selected these three case studies because they display distinct trends of movement over time, including slow, episodic sliding and catastrophic failure, thus allowing ideal benchmarks to verify the accuracy of the proposed framework.

4.2 Parameter optimization method

For the case studies in this paper, model parameters were assessed by optimization procedures focusing on the identification of best fit values for k^b (shear zone permeability), φ (friction angle), and ψ (dilation angle). We used a grid search inverse method to optimize these parameters (Allmendinger, 1998). This method computes the objective function (OBJ) from initial guesses based on typical ranges of these parameters and then searches the minimum OBJ.

$$OBJ = \sum(d_o - d_s(k^b, \varphi, \psi))^2, \quad (19)$$

where d_o is observed displacement; d_s is simulated displacement. The parameters (k^b, φ, ψ) leading to the minimum OBJ will be the optimized ones. Using the Two Towers landslide as an example, (detail given in the next section), we perform a grid search for ψ ranging between 0.5° to 5° (dilation angle for clayey material is limited; Vermeer and de Borst, 1984). The permeability and friction angle for the KJf material has a large range, with permeability ranging from 1.6×10^{-5} to 3×10^{-10} m/s within a single landslide body (Iverson and Major, 1987) and friction angle ranging from 12°~50° (Keefer and Johnson, 1983; Roadifer et al., 2009; Schulz et al., 2018b; Nereson et al., 2018). We also note that studies have shown that the permeability of the shear zone (k^b) is often smaller than the landslide body material (Baum and Reid, 2000; Nereson et al., 2018). Thus, we performed the grid search using permeabilities between 1.6×10^{-7} and 3×10^{-12}. Our parametric

455 analysis provides a narrow band of values (dark blue in Fig. 8) with relatively small OBJ values.

456 Among them, the minimum value can be found. Optimized parameters are displayed in Table 1.

457 **Table 1. Properties and optimized parameters for each case study**

Model parameters	Two Towers	Minor Creek	Mud Creek	Initial values
Area (hectares)	1	10	23	-
Inclination (°)	15	15	32	-
Depth (m)	7	6	20	-
k^b (m/s)	3.3 x10^{-11}	3.3 x10^{-9}	8.8 x10^{-10}	1.6x10^{-7} ~ 3x10^{-12}
φ (°)	22.8	19.3	47.8	12~50
ψ (°)	2	2	0.5	0.5~5

458

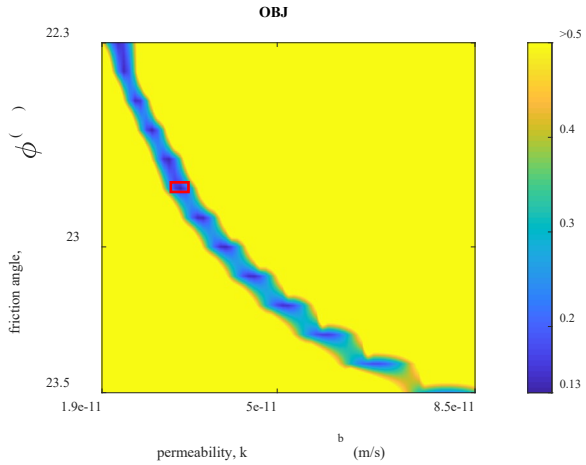

459

460 **Figure 8. Inverse analyses obtained OBJ values corresponding to friction angle and permeability when $\psi = 2°$,**

461 **optimized parameter is indicated by the red polygon.**

462

463 *4.3 Two Towers landslide*

464 The Two Towers landslide (Fig. 7) is around 250 m long and averages about 40 m in width and 7

465 m in depth; with an average inclination of 15° (Schulz et al., 2018a). The thickness of the shear

zone is ~0.5 m (Schulz et al., 2018b). The groundwater head (monitored at multiple sites within the active landslide) and landslide movement (monitored from an inclinometer located at the landslide toe, Fig. 7) were monitored at multiple sites within the active landslide from November 2014 to July 2017 by Schulz et al. (2018a; b). We selected the ground water head measured at the middle of the landslide (Schulz et al., 2018a), in that it is far from the boundaries and can be regarded as the representative descriptor of the hydrologic state for a translational landslide. However, it is important to point out that other options (e.g., the average of all measurement points) would also be viable choices in this modeling context. In the central portion, we used data from the piezometer located at around 5.7 m below the ground, from which the water head above landslide base is reported. The resulting pore-water pressure at the top of the shear zone (p_w^t, Fig. 9a) was then computed for a scenario of downslope seepage and eventually used as boundary condition for the simulation. The cumulative rainfall during the observation period is provided in Fig. 9a. Clay swelling was observed at the site and shown to have played a major role in the landslide dynamics (Schulz et al., 2018a). However, we did not explicitly incorporate clay swelling into our model. We also note that Schulz et al. (2018a) concluded that shear-induced dilation was not evident from their field or laboratory measurements. Nonetheless, our model simulations are here aimed at testing whether dilation can explain the observed motion at the Two Towers site.

Fig. 9a shows the simulated pore-water pressure distribution at the top and bottom of the shear zone, characterized by delayed bottom hydrological response compared to the forcing pore-water pressure imposed at the top of the shear zone (p_w^t and corresponding p_w^{sb}). Although the overall simulated displacement trend is consistent with the monitoring data at the Two Towers landslide site, as Fig 9c shows, a mismatch exists between model results and data. For instance, we find that the simulated movement begins earlier than the observations and underestimates the measured

displacement in 2016 and 2017. Because in our simulation movements are generated by hydraulic forcing, these mismatches can be interpreted as a result inaccuracies in the pore-water pressure simulations. Most notably, the discrepancies between our simulations and the measured motion suggests that shear-induced dilation alone cannot explain the measured landslide response and other mechanisms, such as clay swelling, need to be considered (Schulz et al., 2018a).

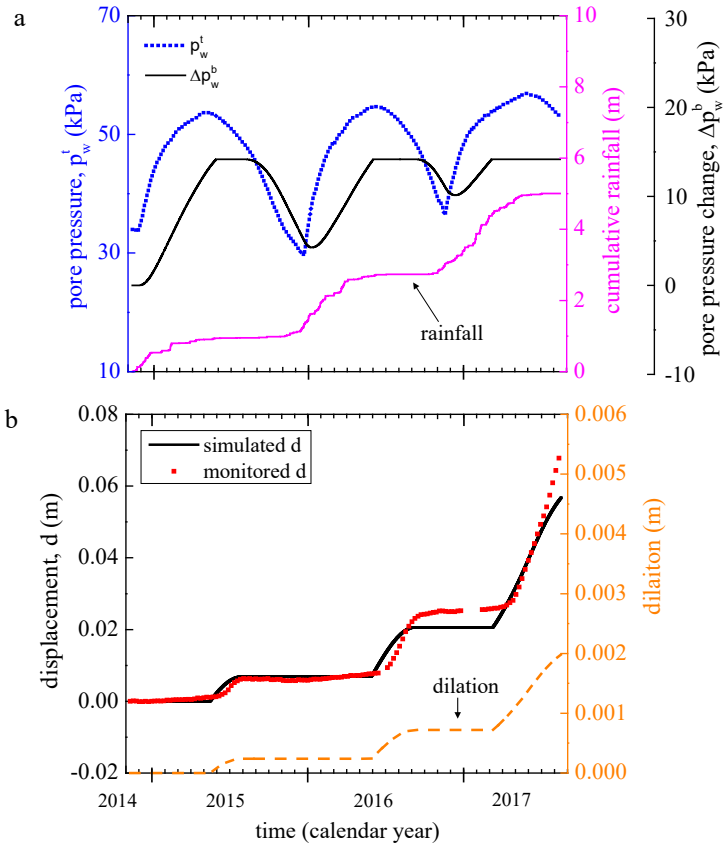

Figure 9. Model and measured data at Two Towers landslide. a) Pore-water pressure change at top of shear zone (Schulz et al., 2018a; b) based on the monitoring of water head above landslide base from a piezometer in the middle of the landslide, optimized pore-water pressure distribution at the bottom of shear zone, and cumulative rainfall. b) computational displacement from optimization compared to the monitored value and simulated normal dilation.

To quantify the movements due to dilation, we also computed the normal displacement (Fig. 9b) predicted by the model during the three-year period considered in this study. The results show an increase in plastic normal strain in correspondence with each episode of motion, with an increasing trend that produces a 2 mm total heave by the end of the considered period. Although not zero, this dilation-induced motion is predicted to be small, thus requiring very accurate measurements to verify the actual extent of dilation at the field scale.

4.3 Minor Creek

Minor Creek landslide (Fig. 7) is a slow-moving landslide covering about 10 hectares in Redwood Creek drainage basin, northern CA Coast Ranges. Iverson and Major (1987) collected three years of detailed rainfall, groundwater and movement data (Fig. 10a and b) of this landslide from October 1982 to September 1985. Iverson (2005) also previously explored the role of shear-induced dilation (with 3° dilation angle) as a key mechanism controlling the slow-moving behavior of Minor Creek. The average slope angle is 15°; the thickness of the landslide along its longitudinal axis is 6 m and the shear zone thickness is 1 m (Iverson and Major, 1987).

Saturated permeability ($k^t = 9\text{x}10^{-7}$ m/s) and storage coefficient ($S_s = 0.45$) of the landslide material can be determined by simulating the monitored pore-water pressure data through trial and error (Fig. 10a). Our calculated diffusivity ($2\text{x}10^{-6}$ m^2/s) and mechanical parameters (Table 1) are similar to the value back calculated by Iverson and Major (1987). Our model can capture much of displacement trend, such as seasonal and year to year changes in displacement magnitude (Fig. 10c), but again we observe significant mismatches between our model results and the observed motion. Like Two Towers, we attribute these mismatches to our simulated pore-water pressure time series which differs significantly from the observed pore-water pressure. We find our model involves a several months delay in the prediction of the activation of the landslide in 1983 and

523 over predicts the total displacement by a factor of 2. Improvements to our hydraulic simulation are
524 needed to better account for these hydrologic changes and could be accomplished by incorporating
525 factors such as evapotranspiration, unsaturated effect, or lateral flow.

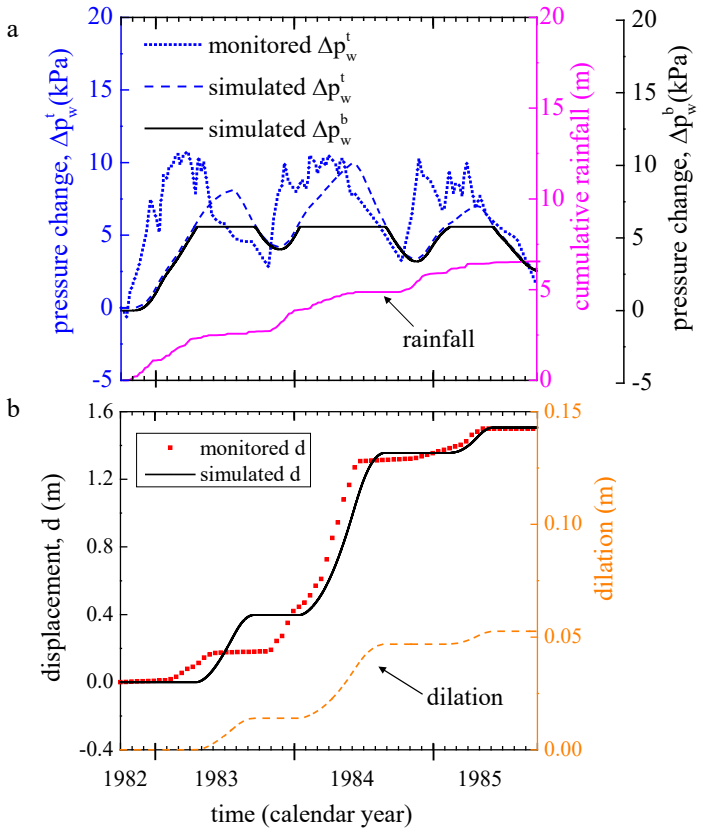

526

527 **Figure 10. Simulated and monitored hydrological and mechanical behaviors at the Minor Creek landslide site.**
528 **a) monitored and simulated pore-water pressure at top of the shear zone, simulated pore-water pressure at the**
529 **base of the shear zone, and cumulative rainfall, c) monitored and simulated displacement, and simulated**
530 **dilation.**

531 *4.4 Mud Creek landslide*

532 Our last test case is the Mud Creek landslide (Fig. 7), central California Coast Ranges. The Mud
533 Creek landslide displayed stable sliding for more than 8 years; however, it suddenly failed
534 catastrophically on a dry day (May 20, 2017) following a prolonged season of heavy rainfall. This

event caused major damage to California State Highway 1 and has been studied through a variety of remote sensing observations and hydrologic models (Handwerger et al., 2019a; Warrick et al., 2019). More than two years of landslide displacement was measured by InSAR before the catastrophic failure occurred and we model these measurements here (Handwerger et al., 2019a).

Mud Creek is characterized by relatively steep terrain with an average slope angle around 32°. We assume the shear zone is located at a depth of 20 m, which is within the range of values measured by Warrick et al., (2019). In this analysis, given the lack of ground based hydraulic observations, the pore-water pressure at the top of the shear zone (p_w^t) is simulated using back-calculated hydraulic parameters $k^t = 3$ x10^{-6} m/s and $S_s = 0.14$ m^{-1} as illustrated in Appendix 2. Using these parameters, the pore-water pressure distribution of Mud Creek landslide can be computed as illustrated by Fig. 11a (affected by the precipitation displayed as Fig. 11b).

The optimization strategy discussed in the previous sections is also used for this case, leading to simulation of both pore-water pressure at bottom of shear zone (Fig. 11a), sliding movement (Fig. 11c), and normal deformation (Fig. 11c). The results are consistent with the InSAR observations prior to the catastrophic collapse. Notably, the optimized friction angle for Mud Creek is very high (about 48°; Table 1), which is an outcome of the steep (i.e., high initial stress ratio), deep-seated slope and nearly fully saturated initial condition (leads to high pore-water pressure). We assume saturated conditions in that field data from other landslide sites in the KJf show that the groundwater table remains within 2-3 m of the ground surface during the dry season and rises to the ground surface during the wet season (Iverson and Major, 1987; Schulz et al., 2018a; Hahm et al., 2019; Finnegan et al., 2021). Our results for Mud Creek provide a better fit of the observations compared to Two Towers and Minor Creek. Yet, mismatches in the predicted temporal evolution of the movements appear in this case study too (e.g., early activation in 2015 and 2016), and once

again can be attributed to the simulated early build-up of pore-water pressure (Fig. 11a). Similar to the previous cases, dilation-induced heave (Fig. 11b) was also computed by tracking the evolution of the plastic normal strain during sliding.

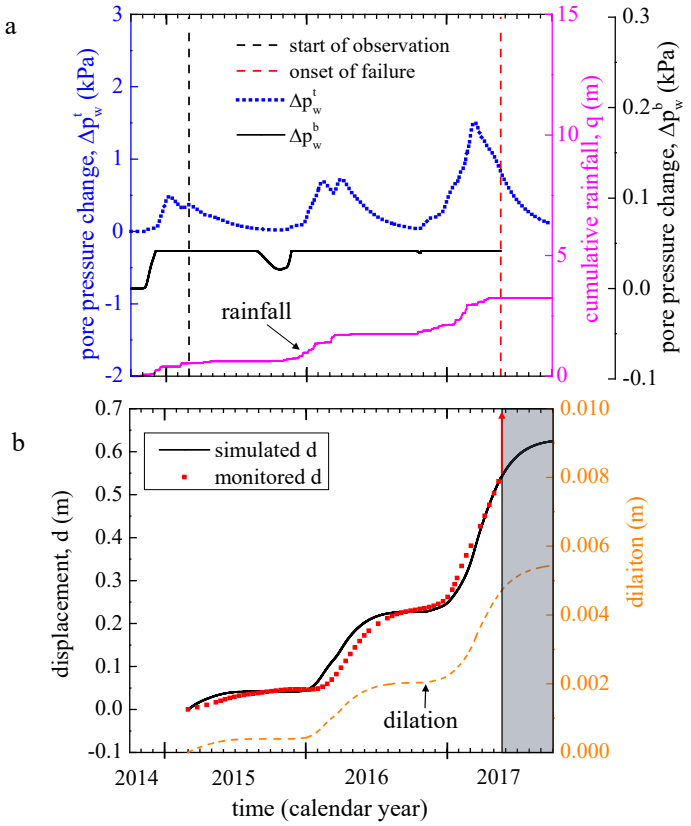

Figure 11. Simulated and monitored hydrological and mechanical behaviors at the Mud Creek landslide site. a) Simulated pore-water pressure distribution at top and bottom of the shear zone and cumulative rainfall, b) monitored and simulated displacement by the end of stable sliding (the left boundary of the shaded rectangle represents the occurrence of catastrophic failure) and simulated normal dilation.

Although Mud Creek landslide did eventually fail catastrophically, a positive dilation angle (with less than 3 mm normal deformation increase, Fig. 11d) is required to capture the pre-failure slow movement. As a result, our model will always predict self-regulating creep. To further emphasize this point (and highlight a key model limitation), we extend the simulation beyond the time at

570 which catastrophic failure was observed in the field, so as to show how the model would have
571 erroneously predicted the motion (Fig. 11b). It can thus be concluded that, to capture runaway
572 acceleration, our model would need to account for vanishing dilative effects (Fig. 6d) (Moore and
573 Iverson, 2002).

574 **5. Discussion**

575 In this manuscript, we developed a hydro-mechanical modeling framework to describe the
576 dynamics of landslides in response to rainfall infiltration. We showed that an elastic-perfectly
577 plastic frictional model enables the simulation of landslide creep in the presence of plastic dilation,
578 as well as of runaway failure due to lack of self-regulating mechanisms (e.g., shear zone having
579 reached critical state or exhibiting plastic contraction; Fig. 6d). While the model can be used to
580 simulate different modes of landslide movement triggered by precipitation, the formulation
581 discussed in the paper cannot capture transitions from stable creep to runaway failure, as illustrated
582 in our case study of the Mud Creek landslide. This finding encourages future model development
583 to account for more realistic constitutive laws based on the critical state theory (Roscoe et al., 1958;
584 Schofield and Wroth, 1968), which would enable the evolution of plastic deformation.

585 We studied three cases of slow-moving landslides located in California. Their velocity changes
586 are governed by precipitation, while different magnitudes of acceleration were observed for each
587 site. The Two Towers landslide exhibited rates from around 0.01 to 0.04 m/yr, while Minor Creek
588 landslide exhibited rates from 0.2 to 1 m/yr with a large increase in displacement during the 1984
589 wet season. The sliding velocity of Mud Creek landslide, before the catastrophic failure, falls in
590 between the above two cases. It is not surprising that the three landslides experienced different
591 magnitudes of sliding movement and exhibited different behaviors. Several factors can lead to this

phenomenon: topography (Table 1), local precipitation (Fig 9c; Fig 10c; Fig. 11c), groundwater hydrology, variations in material properties, stress level (i.e., thickness), and more. Considering these complex conditions, we find it may always be reasonable to use inverse analysis to optimize parameters even when landslides occur within the same region and appear similar.

As for our optimized parameters (Table 1), they all fall in range obtained from laboratory tests or field observations as explained in Section 4.2. Yet, the optimized friction angle of Mud Creek landslide (φ =47.8°) is much larger than values typically observed from laboratory tests on landslide materials. We propose this high back calculated value results from a few reasons: first, we assume the landslide is fully saturated and has zero cohesion. If we accounted for cohesion and lower pore-water pressures this would offset the strength required by the friction angle to maintain stability. Second, Mud Creek landslide was steep (average slope angle 32°) which requires a relatively high friction angle (~30 °) to remain stable during the dry season.

Both the Minor Creek and Two Towers landslides have been the subject of previous investigations and modeling efforts (e.g., Iverson and Major, 1987; Iverson, 2005; Schulz et al., 2018a). Iverson (2005) explained the seasonal dynamics of Minor Creek landslide using a shear-induced dilation model with interfacial hydro-mechanical coupling. In agreement with this prior work, our simulation leads to an acceptable representation of both the magnitude and the rate of sliding, which in all cases displayed the attributes of a stable, self-regulated episodic creep. Moreover, while our analysis enabled for inherent differences between the diffusivity of the landslide material and that of the basal shear zone (the latter being mediated by frictional/dilative properties), the good agreement between our results and those reported by Iverson (2005) suggest that inelastic effects play a limited role in the diffusivity of landslides not yet undergoing runaway motion (i.e., not having reached local shear instability conditions and/or critical state). This argument is also

relevant for more recent extensions of coupled sliding-consolidation analyses specific for multi-dimensional domains (Iverson and George, 2014; George and Iverson, 2014). However, since these approaches also rely on poroelastic diffusivity models, the potential implications of inelastic deformation on the pore-water pressure diffusivity may warrant further study, especially in the presence of liquefied materials (Rice, 1975; Chen and Buscarnera, 2022).

The activation and arrest of Two Towers landslide site was closely examined by Schulz et al. (2018a) through a limit equilibrium method incorporating a new strength coefficient governed by clay swelling. They concluded that the additional strength imparted by swelling effects controlled the lag between the water level fluctuation and landslide activation. In our work, we found that shear-induced dilation can also partially explain the lag between when pore-water pressures above the shear zone rise and when the landslide starts to move, with notable mismatches described above. However, we note again that Schulz et al. (2018a) concluded that neither field measurement nor laboratory tests indicated shear-induced dilation at the Two Towers landslide. These observations warrant questions as to why a dilation model was used in this work. One of the core reasons behind this choice is that dilation is commonly invoked as a key strengthening mechanism that permits slow and stable motion of creeping landslides (Iverson et al., 2000; Iverson, 2005; Agliardi, et al., 2020), and it thus deserves full consideration whenever testing any new hydro-mechanical formulation for the prediction of landslide motion. Hence, one of our key goals was to determine to what extent dilation can explain any of the observed behaviors documented in the literature. Despite the ability of our model to capture the overall trends at the Two Towers site, the difficulty of achieving an accurate match of both hydraulic and mechanical response (paired with the already mentioned challenges of constraining the value of dilation in the field) indicates that dilation alone may not suffice to explain the observed dynamics and must then be studied in conjunction with

638 other processes, such as clay swelling. In our opinion, only fully coupled, deformation-based
639 approaches encompassing all the potential causes of self-regulating motion can definitively reveal
640 which factors play a primary role, as opposed to those that are secondary and may be regarded as
641 inessential to explain field observations. While this more complete analysis was not attempted here,
642 our proposed framework enables future extensions through the incorporation of constitutive laws
643 with suction-induced swelling and other moisture-regulated inelastic processes (Song et al., 2020).

644 While we have shown that the flow-deformation coupling may in part regulate landslide behaviors,
645 there are other widely used models to simulate slow-moving landslides. The most common of these
646 are viscoplastic models (Van Asch et al., 2007; Angeli et al., 1996; Oberender and Puzrin, 2016),
647 which can be used to depict the time-dependent behaviors of earthen materials (Mitchell et al.,
648 1968; Liingaard et al., 2004; Marinelli et al., 2018). Ring shear tests of samples taken from Two
649 Towers landslide showed the friction angle varies ~21° and ~24° with shear rates from 0.01 to 1
650 mm/s (Schulz et al., 2018b). These findings imply some the landslide material exhibits some rate
651 dependency, although at the range of the sliding rates exhibited in the field. It thus indicates that
652 viscoplastic models can be used to capture creeping landslide movement under quasi-static
653 conditions (Li et al., 2023). However, these models may not always be appropriate for landslides
654 forming within earthen materials exhibiting negligible viscosity (Iverson, 2020). In this manuscript,
655 the proposed hydro-mechanical coupled framework was able to describe landslide creep without
656 incorporating earthen material viscosity. Yet, its mathematical formulation does not hinder the
657 possibility of accounting for viscous effects, which can be readily inserted by expressing the
658 inelastic strain rate in Eq. (15) by a viscoplastic flow rule. In a future perspective, this possibility
659 can prove useful to quantify the peak velocity of flow-like landslides (Chen and Buscarnera, 2022),

as well as to replicate temporal patterns of landslide creep more complex than standard episodic slips (Li et al., 2023).

6. Conclusions

We developed a modelling framework enabling the study of rainfall induced landslide dynamics, with the goal to account for the interaction between precipitation, pore-water pressure change, and inelastic deformation within the shear zone of active landslides. Our framework involves two sequential diffusion processes, one within a rigid landslide block and another within an inelastically deformable basal shear zone. While the former is used to simulate hydraulic forcing across the landslide material, the latter enables explicit consideration of the inelasticity of the shear zone material, thus modulating the timescale of sliding and pore-water pressure diffusion through dedicated constitutive laws. Spatial condensation procedures are used to derive a set of coupled ordinary differential equations reflective of the landslide dynamics and accounting for the feedback between transient water flow, inertial movement, and material inelasticity. To illustrate the main characteristics of the proposed framework, the model was linked with a perfectly plastic frictional law enabling dilation and/or contraction of the shear zone material during sliding.

We showed that the model can operate both under elastic and plastic regimes. By suppressing plastic effects, our model is able to simulate delayed hydraulic forcing as a function of the diffusivity of both the landslide material and shear zone. Moreover, we found that sliding can be simulated if the hydraulic forcing drives the effective stress state to the plastic regime. The simulations indicate that the onset of plasticity starts to generate negative excess pore-water pressure, which regulates the sliding dynamics through constitutive feedbacks modulating the effective diffusivity of the basal shear zone. Case studies indicate that distinct types of landslide

682 behaviors can be simulated satisfactorily with reduced computational cost and a limited number
683 of model parameters. Our model framework enables the computation of self-feeding catastrophic
684 failure in the presence of either contractive shear zone material (e.g., liquefaction events) or critical
685 state conditions (i.e., no dilation or contraction) and self-regulating (i.e., dilatative) episodic and/or
686 quasi-steady landslide motion. The main advantage of our proposed framework is the virtually
687 endless opportunities it offers to augment the constitutive description of the shear zone material
688 that can describe various mechanical-hydrologic feedbacks.

689

690 **ACKNOWLEDGEMENTS**

691 This work was supported by Grant No. ICER-1854951 awarded by the U.S. National Science
692 Foundation. Part of this research was carried out at the Jet Propulsion Laboratory, California
693 Institute of Technology, under a contract with the National Aeronautics and Space Administration
694 (80NM0018D0004).

695

696

697 **Appendix 1. Simplification of water mass balance using Parabolic assumption**

698 In this manuscript, in order to solve the 2nd order PDE, $\frac{k^b}{\gamma_w}\frac{\partial^2 p_w}{\partial z^2} + \dot{\varepsilon} = 0$, a parabolic p_w^e (excess
699 pore-water pressure) profile (Wood, 2004) is used to simplify the computation. We write the total
700 pore-water pressure expression:

701 $$p_w = p_w^s + p_w^e, \tag{A1}$$

where p_w^s is the stationary (steady state) pore-water pressure, its value is influenced instantaneously by the applied pore-water pressure at the top of the shear zone. Here, we assume that the p_w^e distributed in a parabolic profile (Wood, 2004) as illustrated in Fig. A1:

$$p_w^e = a\xi^2 + b\xi + c. \quad \text{(A2)}$$

where ξ represents the normal distance from the base of shear zone. We can thus obtain that at the bottom of the shear zone, where $\xi = 0$:

$$c = p_w^{eb} = p_w^b - p_w^{sb}. \quad \text{(A3)}$$

Where the superscript b indicates the pore-water pressures values are for the basal shear zone. While, at the top of the shear zone, $\xi = h_s cos\theta$, $p_w^{et} = 0$ because the top of the shear zone is assumed to be drained (no excess pore-water pressure can be built up), thus:

$$a{h_s}^2 cos^2\theta + bh_s cos\theta + p_w^{eb} = p_w^{et} = 0. \quad \text{(A4)}$$

Meanwhile, the bottom of shear zone is undrained, so that the p_w^e distribution will be symmetric above and below the $\xi = 0$ surface. Therefore, at $\xi = -h_s cos\theta$:

$$a{h_s}^2 cos^2\theta - bh_s cos\theta + p_w^{eb} = 0. \quad \text{(A5)}$$

Adding Eq. A4 with Eq. A5, we get:

$$a = \frac{-p_w^{eb}}{h_s^2 cos^2\theta}. \quad \text{(A6)}$$

As the stationary (steady state) pressure will be changed simultaneously within the whole shear zone, from Eq. A2 and Eq. A6, we can get: $\frac{\partial^2 p_w}{\partial z^2} = \frac{\partial^2 (p_w^e)}{\partial \xi^2} = 2a = 2\frac{p_w^{sb} - p_w^b}{h_s^2 cos^2\theta}$.

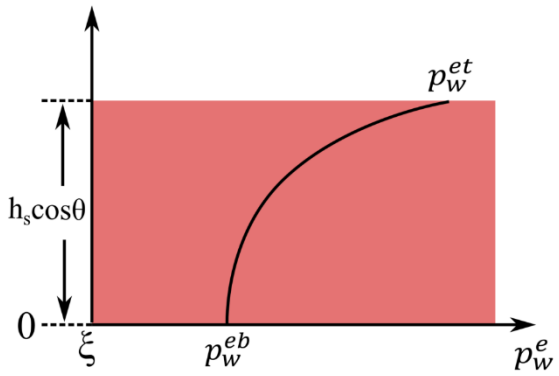

720

721 **Figure A1. Schematic of parabolic distributed p_w^e.**

722

723 **Appendix 2. Hydrological parameter determination of Mud Creek landslide**

724 There are no ground-based observations of pore-water pressure changes for the Mud Creek
725 landslide. In order to obtain the hydrological response for Mud Creek landslide, we used field data
726 from the Minor Creek landslide site to train our hydrological model. Both Minor Creek and Mud
727 Creek landslide located in KJf, we assumed that the sliding surface of them experience similar
728 hydrological changes driven by rainfall. Our assumption is reasonable based on the hydrological
729 observations of KJf at numerous sites throughout California (Iverson and Major, 1987; Schulz et
730 al., 2018a; Hahm et al., 2019; Finnegan et al., 2021).

731 In order to calibrate the model parameters for Mud Creek landslide, we adjusted the simulated
732 landslide thickness for Minor Creek to 20 m thick (i.e., Mud Creek thickness); we then back
733 calculated the parameters that would lead to simulation results that match the Minor Creek
734 observation. Fig. A2 shows the $k^t = 3 \times 10^{-6}$ m/s (saturated permeability of landslide material) and
735 S_s (storage coefficient) changes to 0.14 m^{-1} are reasonable values. The back calculated diffusivity
736 2×10^{-5} m^2/s still falls in the range of estimation.

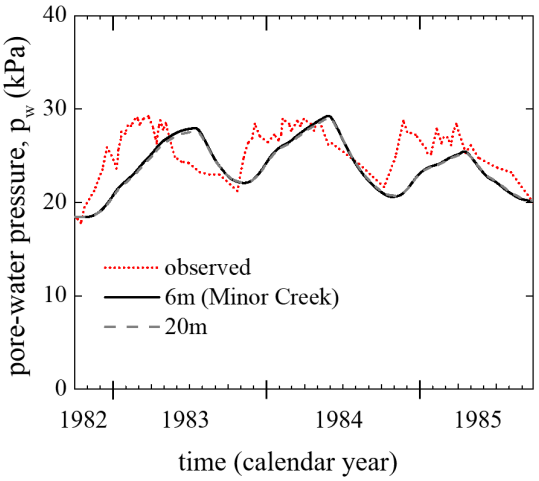

737

738 **Figure A2. Calibration of Mud Creek hydraulic parameters of the landslide material, simulation of Minor**
739 **Creek compared with 20 m depth.**

Reference

Agliardi, F., Scuderi, M. M., Fusi, N., & Collettini, C. (2020). Slow-to-fast transition of giant creeping rockslides modulated by undrained loading in basal shear zones. Nature communications, 11(1), 1-11.

Allmendinger, R. W. (1998). Inverse and forward numerical modeling of trishear fault-propagation folds. Tectonics, 17(4), 640-656.

Alonso, E. E. (2021). Triggering and motion of landslides. Géotechnique, 71(1), 3-59.

Angeli, M.-G., Gasparetto, P., Menotti, R. M., Pasuto, A., & Silvano, S. (1996). A visco-plastic model for slope analysis applied to a mudslide in Cortina d'Ampezzo, Italy. Quarterly Journal of Engineering Geology and Hydrogeology, 29(3), 233-240.

Bailey, E. H., Irwin, W. P., & Jones, D. L. (1964). Franciscan and related rocks, and their significance in the geology of western California. Retrieved from

Bandara, S., Ferrari, A., & Laloui, L. (2016). Modelling landslides in unsaturated slopes subjected to rainfall infiltration using material point method. International Journal for Numerical and Analytical Methods in Geomechanics, 40(9), 1358-1380.

Baum, R., & Reid, M. (2000). *Ground water isolation by low-permeability clays in landslide shear zones.* Paper presented at the Landslides in Research, Theory and Practice: Proceedings of the 8th International Symposium on Landslides held in Cardiff on 26–30 June 2000.

Baum, R. L., Godt, J. W., & Savage, W. Z. (2010). Estimating the timing and location of shallow rainfall-induced landslides using a model for transient, unsaturated infiltration. Journal of Geophysical Research: Earth Surface, 115(F3).

Belmans, C., Wesseling, J. G., & Feddes, R. A. (1983). Simulation model of the water balance of a cropped soil: SWATRE. Journal of Hydrology, 63(3-4), 271-286.

Bennett, G. L., Roering, J. J., Mackey, B. H., Handwerger, A. L., Schmidt, D. A., & Guillod, B. P. (2016). Historic drought puts the brakes on earthflows in Northern California. Geophysical Research Letters, 43(11), 5725-5731.

Berti, M., & Simoni, A. (2010). Field evidence of pore pressure diffusion in clayey soils prone to landsliding. Journal of Geophysical Research: Earth Surface, 115(F3).

Buscarnera, G., & Di Prisco, C. (2011). Stability criteria for unsaturated shallow slopes. Géotechnique Letters, 1(4), 85-90.

Buscarnera, G., & Whittle, A. J. (2012). Constitutive modelling approach for evaluating the triggering of flow slides. Canadian Geotechnical Journal, 49(5), 499-511.

Cascini, L., Calvello, M., & Grimaldi, G. M. (2010). Groundwater modeling for the analysis of active slow-moving landslides. Journal of Geotechnical and Geoenvironmental Engineering, 136(9), 1220-1230.

Chen, Y., & Buscarnera, G. (2021). Numerical simulation of unstable suction transients in unsaturated soils: the role of wetting collapse. International Journal for Numerical and Analytical Methods in Geomechanics, 45(11), 1569-1587.

Chen, Y., & Buscarnera, G. (2022). Unified modeling framework of flowslide triggering and runout. Géotechnique, 1-37.

Cohen-Waeber, J., Bürgmann, R., Chaussard, E., Giannico, C., & Ferretti, A. (2018). Spatiotemporal patterns of precipitation-modulated landslide deformation from independent component analysis of InSAR time series. Geophysical Research Letters, 45(4), 1878-1887.

Conte, E., Donato, A., & Troncone, A. (2014). A finite element approach for the analysis of active slow-moving landslides. Landslides, 11(4), 723-731.

Corominas, J., Moya, J., Ledesma, A., Lloret, A., & Gili, J. A. (2005). Prediction of ground displacements and velocities from groundwater level changes at the Vallcebre landslide (Eastern Pyrenees, Spain). Landslides, 2(2), 83-96.

Corominas, J., Moya, J., Lloret, A., Gili, J., Angeli, M., Pasuto, A., & Silvano, S. (2000). Measurement of landslide displacements using a wire extensometer. Engineering geology, 55(3), 149-166.
Davis, R. O., & Selvadurai, A. P. (2005). Plasticity and geomechanics: Cambridge university press.
Di Prisco, C., Mancinelli, L., Zanelotti, L., & Pisanò, F. (2015). Numerical stability analysis of submerged slopes subject to rapid sedimentation processes. Continuum Mechanics and Thermodynamics, 27(1), 157-172.
Finnegan, N., Perkins, J., Nereson, A., & Handwerger, A. (2021). Unsaturated Flow Processes and the Onset of Seasonal Deformation in Slow-Moving Landslides. Journal of Geophysical Research: Earth Surface, 126(5), e2020JF005758.
fr/MIDI/, G. M. g. p. u.-m. f. h. w. l. u.-m. (2004). On dense granular flows. The European Physical Journal E, 14, 341-365.
George, D. L., & Iverson, R. M. (2014). A depth-averaged debris-flow model that includes the effects of evolving dilatancy. II. Numerical predictions and experimental tests. Proceedings of the Royal Society A: Mathematical, Physical and Engineering Sciences, 470(2170), 20130820.
Hahm, W. J., Rempe, D. M., Dralle, D. N., Dawson, T. E., Lovill, S. M., Bryk, A. B., . . . Dietrich, W. E. (2019). Lithologically controlled subsurface critical zone thickness and water storage capacity determine regional plant community composition. Water Resources Research, 55(4), 3028-3055.
Handwerger, A. L., Fielding, E. J., Huang, M. H., Bennett, G. L., Liang, C., & Schulz, W. H. (2019). Widespread initiation, reactivation, and acceleration of landslides in the northern California Coast Ranges due to extreme rainfall. Journal of Geophysical Research: Earth Surface, 124(7), 1782-1797.
Handwerger, A. L., Fielding, E. J., Sangha, S. S., & Bekaert, D. P. (2022). Landslide sensitivity and response to precipitation changes in wet and dry climates. Geophysical Research Letters, e2022GL099499.
Handwerger, A. L., Huang, M.-H., Fielding, E. J., Booth, A. M., & Bürgmann, R. (2019). A shift from drought to extreme rainfall drives a stable landslide to catastrophic failure. Scientific reports, 9(1), 1-12.
Handwerger, A. L., Roering, J. J., & Schmidt, D. A. (2013). Controls on the seasonal deformation of slow-moving landslides. Earth and Planetary Science Letters, 377, 239-247.
Hendron Jr, A., & Patton, F. D. (1985). The vaiont slide. A geotechnical analysis based on new geologic observations of the failure surface. Volume 1. Main text. Retrieved from
Hilley, G. E., Bürgmann, R., Ferretti, A., Novali, F., & Rocca, F. (2004). Dynamics of slow-moving landslides from permanent scatterer analysis. Science, 304(5679), 1952-1955.
Hutchinson, J. (1986). A sliding–consolidation model for flow slides. Canadian Geotechnical Journal, 23(2), 115-126.
Iverson, R. M. (2000). Landslide triggering by rain infiltration. Water Resources Research, 36(7), 1897-1910.
Iverson, R. M. (2005). Regulation of landslide motion by dilatancy and pore pressure feedback. Journal of Geophysical Research: Earth Surface, 110(F2).
Iverson, R. M. (2020). Landslide disparities, flume discoveries, and Oso despair. Perspectives of Earth and Space Scientists, 1(1), e2019CN000117.
Iverson, R. M., & George, D. L. (2014). A depth-averaged debris-flow model that includes the effects of evolving dilatancy. I. Physical basis. Proceedings of the Royal Society A: Mathematical, Physical and Engineering Sciences, 470(2170), 20130819.
Iverson, R. M., & Major, J. J. (1987). Rainfall, ground-water flow, and seasonal movement at Minor Creek landslide, northwestern California: Physical interpretation of empirical relations. Geological Society of America Bulletin, 99(4), 579-594.
Iverson, R. M., Reid, M., Iverson, N. R., LaHusen, R., Logan, M., Mann, J., & Brien, D. (2000). Acute sensitivity of landslide rates to initial soil porosity. Science, 290(5491), 513-516.
Keefer, D. K., & Johnson, A. M. (1983). Earth flows; morphology, mobilization, and movement (2330-7102). Retrieved from

Kelsey, H., Coghlan, M., Pitlick, J., & Best, D. (1996). Geomorphic analysis of streamside landslides in the Redwood Creek basin, northwestern California. Paper presented at the International Journal of Rock Mechanics and Mining Sciences and Geomechanics Abstracts.

Lacroix, P., Handwerger, A. L., & Bièvre, G. (2020). Life and death of slow-moving landslides. Nature Reviews Earth & Environment, 1-16.

Leroueil, S. (2001). Natural slopes and cuts: movement and failure mechanisms. Géotechnique, 51(3), 197-243.

Li, X., Lizárraga, J. J., & Buscarnera, G. (2021). Regional-scale simulation of flowslide triggering in stratified deposits. Engineering geology, 292, 106248.

Liingaard, M., Augustesen, A., & Lade, P. V. (2004). Characterization of models for time-dependent behavior of soils. International Journal of Geomechanics, 4(3), 157-177.

Lizárraga, J. J., & Buscarnera, G. (2019). Spatially distributed modeling of rainfall-induced landslides in shallow layered slopes. Landslides, 16(2), 253-263.

Mansour, M. F., Morgenstern, N. R., & Martin, C. D. (2011). Expected damage from displacement of slow-moving slides. Landslides, 8(1), 117-131.

McDougall, S., & Hungr, O. (2004). A model for the analysis of rapid landslide motion across three-dimensional terrain. Canadian Geotechnical Journal, 41(6), 1084-1097.

Marinelli, F., Pisanò, F., Di Prisco, C., & Buscarnera, G. (2018). Model-based interpretation of undrained creep instability in loose sands. Géotechnique, 68(6), 504-517.

Mitchell, J. K., Campanella, R. G., & Singh, A. (1968). Soil creep as a rate process. Journal of the Soil Mechanics and Foundations Division, 94(1), 231-253.

Mihalache, C., & Buscarnera, G. (2016). Diffusive instability of pore pressure transients in deformable unsaturated soils. Journal of Engineering Mechanics, 142(11), 04016091.

Moore, P. L., & Iverson, N. R. (2002). Slow episodic shear of granular materials regulated by dilatant strengthening. Geology, 30(9), 843-846.

Nappo, N., Peduto, D., Mavrouli, O., van Westen, C. J., & Gullà, G. (2019). Slow-moving landslides interacting with the road network: Analysis of damage using ancillary data, in situ surveys and multi-source monitoring data. Engineering geology, 260, 105244.

Nereson, A., Davila Olivera, S., & Finnegan, N. (2018). Field and Remote-Sensing Evidence for Hydro-mechanical Isolation of a Long-Lived Earthflow in Central California. Geophysical Research Letters, 45(18), 9672-9680.

Oberender, P. W., & Puzrin, A. M. (2016). Observation-guided constitutive modelling for creeping landslides. Géotechnique, 66(3), 232-247.

Obrzud, R. (2010). The hardening soil model: A practical guidebook: Zace Services.

Pastor, M., Martin Stickle, M., Dutto, P., Mira, P., Fernández Merodo, J., Blanc, T., Benítez, A. (2015). A viscoplastic approach to the behaviour of fluidized geomaterials with application to fast landslides. Continuum Mechanics and Thermodynamics, 27(1), 21-47.

Petley, D., Mantovani, F., Bulmer, M., & Zannoni, A. (2005). The use of surface monitoring data for the interpretation of landslide movement patterns. Geomorphology, 66(1-4), 133-147.

Puzrin, A. M., & Schmid, A. (2011). Progressive failure of a constrained creeping landslide. Proceedings of the Royal Society A: Mathematical, Physical and Engineering Sciences, 467(2133), 2444-2461.

Rice, J. R. (1975). On the stability of dilatant hardening for saturated rock masses. Journal of Geophysical Research, 80(11), 1531-1536.

Roadifer, J. W., Forrest, M. P., & Lindquist, E. (2009). Evaluation of shear strength of mélange foundation at Calaveras Dam. Paper presented at the Proceedings of the 29th US Soc. for Dams, Annual Meeting and Conference:"Managing our Water Retention Systems", April.

Roering, J. J., Mackey, B. H., Handwerger, A. L., Booth, A. M., Schmidt, D. A., Bennett, G. L., & Cerovski-Darriau, C. (2015). Beyond the angle of repose: A review and synthesis of landslide processes in response to rapid uplift, Eel River, Northern California. Geomorphology, 236, 109-131.

Roscoe, K. H., Schofield, A., & Wroth, a. P. (1958). On the yielding of soils. Géotechnique, 8(1), 22-53.

Rutte, D., Garber, J., Kylander-Clark, A., & Renne, P. R. (2020). An exhumation pulse from the nascent Franciscan subduction zone (California, USA). Tectonics, 39(10), e2020TC006305.
Scheingross, J. S., Minchew, B. M., Mackey, B. H., Simons, M., Lamb, M. P., & Hensley, S. (2013). Fault-zone controls on the spatial distribution of slow-moving landslides. Bulletin, 125(3-4), 473-489.
Schofield, A. N., & Wroth, P. (1968). Critical state soil mechanics (Vol. 310): McGraw-hill London.
Schulz, W. H., Smith, J. B., Wang, G., Jiang, Y., & Roering, J. J. (2018). Clayey landslide initiation and acceleration strongly modulated by soil swelling. Geophysical Research Letters, 45(4), 1888-1896.
Schulz, W., Smith, J., Wang, G., Jiang, Y., Deuell, A., Reeves, R., . . . Roering, J. (2018). Data from in-situ landslide monitoring, Trinity county, California. *US Geol. Survey, Reston, VA, USA*.
Siman-Tov, S., & Brodsky, E. E. (2021). Distinguishing between rheophysical regimes of fluid-saturated granular-flows using dilatancy and acoustic emission measurements. Granular Matter, 23(2), 1-11.
Sloan, S. W., & Abbo, A. J. (1999). Biot consolidation analysis with automatic time stepping and error control Part 1: theory and implementation. International Journal for Numerical and Analytical Methods in Geomechanics, 23(6), 467-492.
Soga, K., Alonso, E., Yerro, A., Kumar, K., & Bandara, S. (2016). Trends in large-deformation analysis of landslide mass movements with particular emphasis on the material point method. Géotechnique, 66(3), 248-273.
Song, Z., Li, X., Lizárraga, J. J., Zhao, L., & Buscarnera, G. (2020). Spatially distributed landslide triggering analyses accounting for coupled infiltration and volume change. Landslides, 17(12), 2811-2824.
Song, Z., Li, X., Lizárraga, J. J., Zhao, L., & Buscarnera, G. (2021). Shallow landslide triggering in unsaturated vegetated slopes: Efficient computation of susceptibility maps. Computers & Geosciences, 154, 104826.
Swain, D. L. (2021). A shorter, sharper rainy season amplifies California wildfire risk. Geophysical Research Letters, 48(5), e2021GL092843.
Tan, Q.-M. (2011). Dimensional analysis: with case studies in mechanics: Springer Science & Business Media.
Terzaghi, K. (1925). Principles of soil mechanics. Engineering News-Record, 95(19-27), 19-32.
Van Asch, T. W., Van Beek, L., & Bogaard, T. (2007). Problems in predicting the mobility of slow-moving landslides. Engineering geology, 91(1), 46-55.
Vermeer, P. A., & De Borst, R. (1984). Non-associated plasticity for soils, concrete and rock. HERON, 29 (3), 1984.
Voight, B. (1978). Rockslides and avalanches: Elsevier Scientific Pub. Co.
Warrick, J. A., Ritchie, A. C., Schmidt, K. M., Reid, M. E., & Logan, J. (2019). Characterizing the catastrophic 2017 Mud Creek landslide, California, using repeat structure-from-motion (SfM) photogrammetry. Landslides, 16(6), 1201-1219.
Wen, T., Tang, H., Wang, Y., Lin, C., & Xiong, C. (2017). Landslide displacement prediction using the GA-LSSVM model and time series analysis: a case study of Three Gorges Reservoir, China. Natural Hazards and Earth System Sciences, 17(12), 2181-2198.
Wood, D. M. (2004). Geotechnical Modelling (Applied geotechnics; v. 1): Taylor & Francis Group/Books.
Wu, L.-Z., Selvadurai, A. P. S., Zhang, L. M., Huang, R.-Q., & Huang, J. (2016). Poro-mechanical coupling influences on potential for rainfall-induced shallow landslides in unsaturated soils. Advances in water resources, 98, 114-121.
Zienkiewicz, O. C., Taylor, R. L., Taylor, R. L., & Taylor, R. L. (2000). The finite element method: solid mechanics (Vol. 2): Butterworth-heinemann.